Electrothermally Actuated Lens Scanner and Latching Brake for Free-Space Board-to-Board Optical Interconnects

Jeffrey B. Chou, Kyoungsik Yu, and Ming C. Wu, *Fellow, IEEE*

Abstract—The design, fabrication, and characterization of an electrothermally actuated lens scanner with bistable mechanical brakes, for the application of free-space board-to-board optical interconnects, are presented. An electrothermally actuated stepper motor is used to scan a 2.8-mm-diameter lens shuttle by a maximum of ± 170 μm ($\pm 1.57°$ scanning angle). Bistable mechanical brakes, toggled with U-shaped thermal actuators, will grip and hold the lens shuttle in place while dissipating zero power. The minimum frictional braking force and maximum actuator force are both measured to be 0.75 mN. A position sensing detector is used to accurately measure the dynamics of the stepper motor and lens system, from which we verify our analytical model. Long-term testing results and solutions are also presented. We demonstrate a robust 10-Gb/s optical link capable of maintaining connection despite a board tilting of $0.45°$ while dissipating zero power. [2012-0013]

Index Terms—Bistable, brake pad, electrothermal actuator, free-space optics, friction, long-term testing, optical interconnect, stepper motor, U shaped.

I. INTRODUCTION

AS THE amount of data processed in the world continues to grow with multicore architectures, datacenters, and cloud computing, the linking technology behind it all has become increasingly critical. Bulky, bandwidth limited, and power hungry electrical interconnects continue to provide the main communication pathway for modern blade server systems [1]. Current board-to-board electrical interconnects have long path lengths ($\sim$30 cm) due to routing via a common backplane. With the wiring bandwidth proportional to A/L^2, where A is the wire cross-sectional area and L is the wire length, the long length of board-to-board systems fundamentally limits the maximum bandwidth of electrical interconnects [2].

Optical interconnects have no such physical limitation, and with a 10×10 array of commercially available 10-Gb/s vertical cavity surface-emitting lasers (VCSELs), a bandwidth of 1 Tb/s can be readily achieved today.

The same backplane used for electrical interconnects also significantly impedes the airflow needed to cool the blades, which severely degrades the cooling efficiency and increases the overall power consumption. Cooling fans require a significant percentage of the overall power consumed in blade server systems [3]. The high power is needed because only 14% of the entire backplane is used for airflow, while the remaining 86% blocks airflow for electrical wiring [4]. To appreciate the massive scale of blade power consumption, it is estimated that, in 2012, the global cost to power all 42 million blade units alone will be 1.2 billion dollars [1]. By eliminating the backplane and using free-space optical interconnects, the cooling efficiency can be significantly increased and potentially save hundreds of millions of dollars in energy spending per year.

Although free-space optical interconnects have been reported in the laboratory environment [5]–[10], one major issue preventing optics from full commercial deployment is optical alignment. The small areas of high-speed 10-Gb/s photodetectors (PDs) ($\sim$25 μm radius) cause the optical system to be very sensitive to board misalignments. Microelectromechanical systems (MEMS) optical lens and mirror scanners offer potential solutions for onboard optical alignment [11]–[25]. Previous attempts to specifically create an autoaligning optical interconnect system correct for fast dynamic lateral displacements with lens scanners and piezoelectric microstages [26], [27]. However, recent results suggest that dynamic misalignments due to vibrations and thermal expansions are negligible, and rather, only large static misalignments due to board insertion are problematic [4]. A passive optical telecentric lens setup is used, which allows for misalignment immunity from lateral displacements smaller than $+/-1$ mm across a board-to-board spacing of 2.5 cm [4]. However, small ($> 0.1°$) angular board tilt misalignment will sever the link in a telecentric optical system.

Since server boards are not designed for precise optical alignment, they can have static tilt in the vertical angles. Our recent measurements show that the boards can tilt by as much as $0.4°$ in repeated insertions. In this paper, we report on an electrothermally actuated microlens scanner with a lens diameter of 2.8 mm and a maximum scan angle of $1.57°$ (170-μm lens displacement). Furthermore, we have integrated a bistable latch to fix the lens position once the optical beam is aligned, thus eliminating the additional power consumption of the MEMS aligner during static conditions. Using the MEMS aligner,

J. B. Chou and M. C. Wu are with the Department of Electrical Engineering and Computer Sciences, University of California at Berkeley, Berkeley, CA 94720 USA (e-mail: scjjchou@eecs.berkeley.edu; wu@eecs.berkeley.edu).

K. Yu is with the Department of Electrical Engineering, Korean Advanced Institute of Science and Technology, Daejeon 305-701, Korea (e-mail: ksyu@kaist.edu).

Color versions of one or more of the figures in this paper are available online at http://ieeexplore.ieee.org.
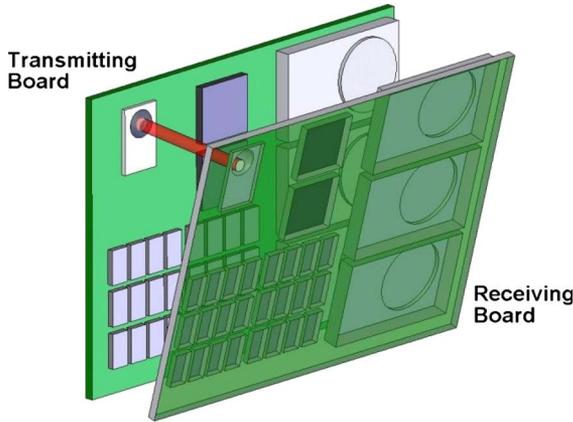
Fig. 1.   Schematic diagram of a free-space board-to-board optical link.

we demonstrate a free-space optical interconnect operating at 10 Gb/s using a VCSEL source. Due to the large optical aperture, the microlens scanner can correct the tilt of an array of parallel VCSEL links.

II. TELECENTRIC OPTICAL SETUP

The schematic of the blade server system with a free-space optical link is shown in Fig. 1. Two lenses, each on the transmitting and receiving boards, are shown to demonstrate the link and serve as the basis from which our optical setup is based upon.

The optical setup used in our MEMS-based free-space optical link is shown in Fig. 2(a), with a MEMS-mounted transmitting lens ($f_1 = 6.2$ mm and $d = 2.8$ mm) and an identical receiving lens. The VCSEL source is placed at the back focal plane of the transmitting lens. Previous optical simulation results and spot diagrams verify that the passive optical setup is immune to lateral ($X-Y$) and optical axis (Z) displacements but highly sensitive to tilt displacements [4]. Our own measurements verify that our optical system maintains alignment despite ± 1-mm displacements in the X-/Y-/Z-directions. This effect can be explained by noticing that a shift in the $X-Y$ plane or Z-direction of the receiving board does not change the input angle of the collimated input light. As a result, the location of the focal point will not be affected relative to the lens. Since the board and the lens are fixed together, the relative position of the focus point will not change due to $X-Y$ or Z motions of the receiving board. There will, of course, be clipping losses if the displacement is larger than the lens diameter, but we will assume that we are working with relatively small distances.

If the boards are tilted relative to each other by an angle θ, as in Fig. 2(b), the input angle of the light to the receiving lens will change, thus shifting the location of the focal point. If the MEMS lens scanner is displaced in the positive Y-direction, by $\Delta y = \theta f_1$, the tilt can be corrected and eliminate the spot shift. For example, to correct for a board tilt well beyond the acceptable range of $\theta = 1°$, the lens must be displaced by $\Delta y = 106$ μm. If a displacement in all three degrees of freedom occurs simultaneously ($Y-Z$ plane, Z-axis, and tilt), only the tilt component will shift the spot location, allowing our system to correct for all three primary causes of misalignments
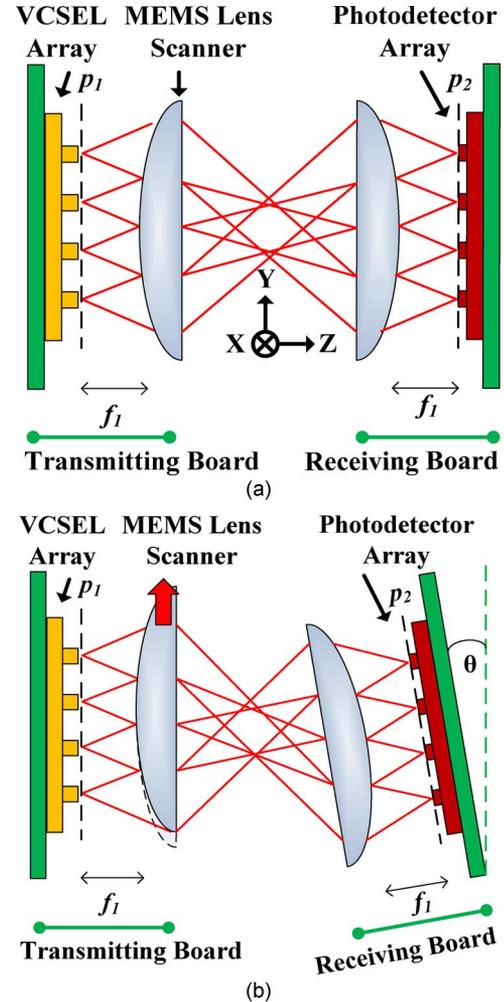

Fig. 2.   Simple diagram of the optical system. (a) Perfectly aligned board-to-board system. (b) Misalignment of tilted board corrected by shifted lens scanner.

TABLE I
MEASURED OPTICAL MISALIGNMENTS IN BOARD SYSTEMS

Misalignment Description	Tolerance
Vibrations	< 1 μm
Static Δy	20 μm
Static Δx	200 μm
Board Tilt	< 0.4°

simultaneously. The measured misalignments in actual blade server systems are listed in Table I.

III. MEMS DESIGN

The 3-D to scale schematic of the entire MEMS lens scanner is shown in Fig. 3. The stepper motors, bistable brakes, springs, and large lens are shown.

A. Spring Design

The device is designed to be operated in the y-axis orientation as in Fig. 2; thus, the spring stiffness was designed to account for the downward force of gravity ($-y$-direction) by allowing the lens to sag down 25 μm due to the weight of the
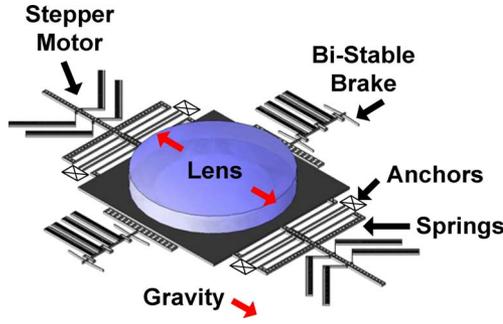
Fig. 3. Schematic diagram of electrothermal lens scanner with bistable brakes. The lens has a diameter of $d = 2.8$ mm.
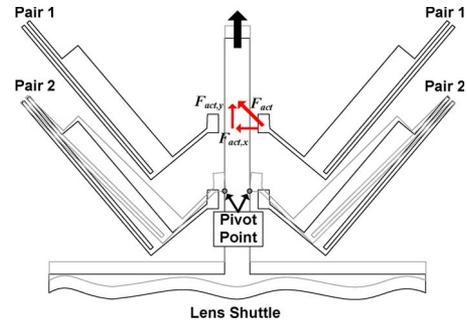

Fig. 4. Schematic view of stepper motor with two alternating pairs of thermal actuators gripping and pushing the lens shuttle upward. The light gray lines represent the engagement of the second pair of actuators to the shuttle. The pivot point refers to the point at which the actuators make contact with the shuttle and tends to roll about when pushing the shuttle.

large lens. The geometry of the lens has a diameter of 2.79 mm and a thickness of 1.93 mm. With the density of the lens being 3800 kg/m^3, the mass of the lens is calculated to be 45 mg. For the spring to support the lens at a 25-μm sag due to gravity, the device requires a total spring stiffness of 9.3 N/m. The finite-element analysis of the actual springs used results in a total spring constant of 9.44 N/m. Assuming the lens to be the dominant mass of the system, the resonant frequency is simulated to be 73 Hz.

The geometry of the scanner was designed to allow for a maximum displacement of 170 μm, limited by the placement of the anchors. Due to this large displacement, the folded flexure spring design was chosen for its large linear deflection range [28]. Fig. 3 shows four folded flexures in parallel which are used to suspend the lens shuttle, minimize displacements in the X-direction, and allow motion in the Y-direction. The large size and mass of the lens cause the device to be very susceptible to motions in the out of plane, Z-direction, but these effects are mitigated in one direction by the back-side handle wafer. For the opposite Z-direction, a form of external packaging could be placed to also mitigate motion in this direction.

B. Electrothermal U-Shaped Actuator

The same bulk-micromachined electrothermal actuators are used in both the stepper motor and the bistable break and is shown in Fig. 3. The basic theory of operation is to use the asymmetrical resistances of the U-shaped actuator to create a temperature difference between the thin "hot" and wide "cold" arms. As the "hot" arm heats up due to joule heating, it thermally expands and causes the entire actuator to bend toward the "cold" arm. Finite-element modeling (FEM) of our thermal actuator evaluates a peak temperature of 1200 K with a displacement of 63.3 μm. The stiffness of the actuator in the pushing direction is simulated to be 30 N/m, which corresponds to a maximum pushing force of 1.9 mN per actuator. An array of 10 μm $\times$ 10 μm squares is etched into the wider "cold" arm to assist in the HF vapor release. Prior work done by Qiu *et al.* on bulk-micromachined thermal actuators used patterned metal to change the electrical conductivity within the actuator [29]. Our actuators use no metal and are lithographically defined to achieve the desired conductivity by varying the cross-sectional area of each arm. As a result of the lack of metal, the design is dependent on the total resistance of the actuator. To minimize
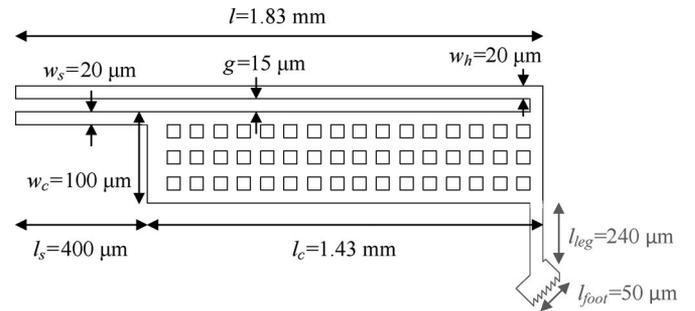

Fig. 5. Schematic and dimensions of the thermal actuators used in the MEMS stepper motor design. This actuator is used for both the bistable brake and the stepper motor. The former uses an extended leg and foot to enhance pushing displacement, as shown in the gray line.

current, a low room temperature resistivity of 0.013 $\Omega \cdot$cm is chosen to meet the current limits of our electrical drivers. However, as the temperature of the actuator increases to high values, the effective resistivity will increase due to increased lattice scattering. A displacement requirement of approximately 50 μm for the actuator stems from the needs of the bistable break.

C. Electrothermal Stepper Actuator

Our device presents a metal-less bulk-micromachined electrothermal stepper motor actuator for high-force and large-displacement purposes, as shown in Fig. 4. Previous successful inchworm designs include an electrostatic bulk-micromachined actuator [30], surface-micromachined thermal actuators [31], [32], and bulk-micromachined V-shaped metalized thermal actuators [33].

To enable the stepper motor, the U-shaped thermal actuator is slightly modified to include a short flexure leg and contact foot, shown in Fig. 5. The compliant flexures allow the leg to bend, and the contact pads increase the contact surface area with the shuttle. When pushing the shuttle upward, the contact pad will rotate about the pivot point, while the opposite corner along the shuttle will lift away slightly from the shuttle. If the flexures were not present, and the U-shaped actuators made direct contact with the shuttle, the combined shuttle–actuator mechanical system would be too rigid, thus preventing the shuttle from moving effectively. Results by Pai and Tien show
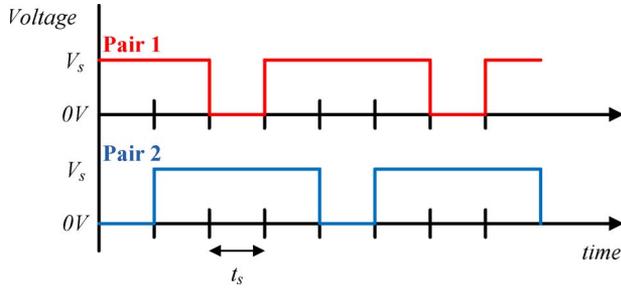
Fig. 6.   Voltage timing diagram for the stepper motor.

TABLE II
BISTABLE BRAKE PARAMETERS

Parameter	Value
h_{bs}	30 μm
L_{bs}	1.1 mm
t_{bs}	5 μm
W_{bs} (Device Layer)	50 μm
F_{close}	2.9 mN
F_{open}	1.45 mN

that direct rigid contact with the shuttle can cause a backward motion at high currents, which would limit the maximum power in the forward motion [32].

The actuators step the shuttle by alternating two pairs of thermal actuators in a grip-and-push scheme and make contact with the shuttle at a 45° angle. The voltage timing diagram is shown in Fig. 6, where V_s is the voltage applied to each pair of actuators and t_s is the time of one "step," where one period is equal to $4t_s$.

To determine the theoretical maximum travel distance, we must take into account the force lost due to the gap distance (10 μm) that the actuator must travel before coming into contact with the shuttle. For example, if we linearly extrapolate the force versus displacement curve from the FEM-simulated values, we can deduce that the maximum force decreases from 1.9 to 1.6 mN per actuator. Using this force value, the force in the y-direction $F_{act,y}$ in Fig. 4 is calculated to be 1.13 mN assuming a 45° contact angle. Since there are two actuators, the total force in the y-direction is 2.26 mN. With the total y-direction force and the theoretical spring constant of the shuttle, the maximum theoretical displacement is calculated to be 243 μm. Due to the compact size of the actuator, large numbers of actuators can be used in parallel to increase the total pushing force.

D. Bistable Break

Curved bistable mechanical structures driven by electrothermal actuators are used to toggle the brake pad between open and closed states [29]. Previous work by Grade *et al.* successfully demonstrates a latchable MEMS brake pad driven with electrostatic comb drives [34]. A bistable brake offers the advantage of zero static power dissipation once the brake is engaged. A schematic of the bistable structure and a table of its parameters are shown in Fig. 7(a) and (b) and Table II, respectively.

The theoretical minimum forces required to flip the bistable structure to the closed and open positions are given by $F_{close} = 2.9$ mN and $F_{open} = 1.45$ mN, respectively. Experimentally,
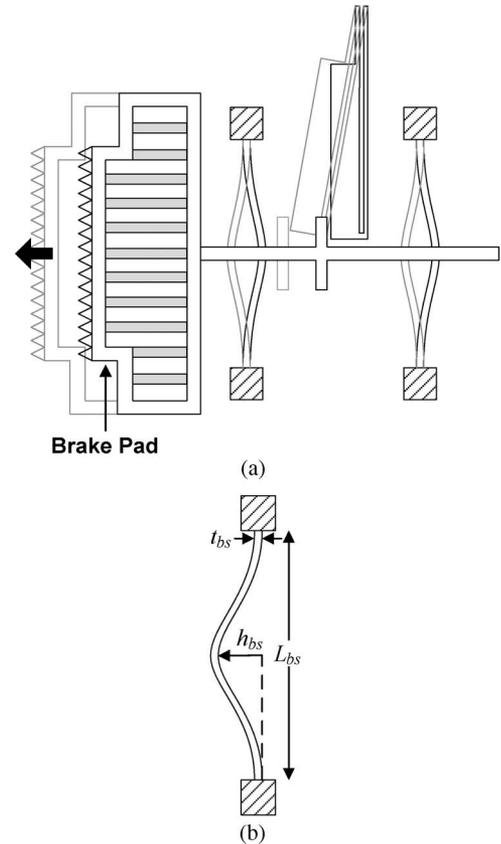

Fig. 7.   (a) Schematic of the curved bistable structure and brake pad used for the brake. The light gray line represents the second stable state of the brake. (b) Schematic view of bistable structure with labels corresponding to those in Table II.

we find that the force generated by two thermal actuators is sufficient to toggle the brakes.

The brake pad is designed to maximize the surface area contact with the lens shuttle, in order to increase the overall frictional forces. Several iterations of the pad were fabricated, and we experimentally found that a large rigid structure provided the best braking performance. Thus, we placed rigid bars inside the brake pad frame to increase the stiffness. A second critical feature required for the brake is the implementation of small 3-μm-pitch triangular teeth at the brake pad/lens frame interface. Once engaged, the brake pad's teeth would interlock with those on the lens frame and significantly increase the frictional forces. Devices without teeth were found to be ineffective as slipping prevented the brakes from functioning.

IV. FABRICATION AND ASSEMBLY

The MEMS device is fabricated via bulk micromachining of a silicon-on-insulator wafer, with a device layer thickness of 50 μm and a buried oxide thickness of 2 μm; illustrations of the fabrication steps are shown in Fig. 8. A single front-side mask is used to define the entire MEMS device for deep reactive-ion etching (DRIE) of the device layer. Scanning electron microscope images reveal an approximately 90° vertical sidewall etch profile along the entire depth of the device, with a maximum of 10 : 1 aspect ratio. A back-side through-wafer etch is performed

(a) (b) (c) (d)
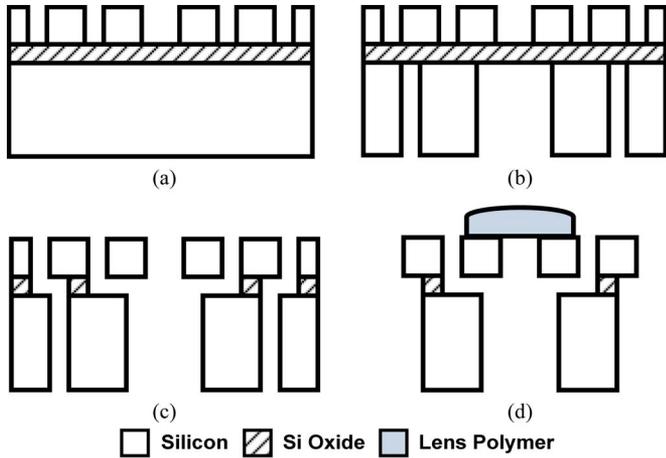
☐ Silicon ▨ Si Oxide ▨ Lens Polymer

Fig. 8. Fabrication steps. (a) Front-side silicon etch. (b) Back-side through-wafer DRIE. (c) HF vapor release etch, which also causes automatic dicing [35]. (d) Lens assembly on the MEMS structure.
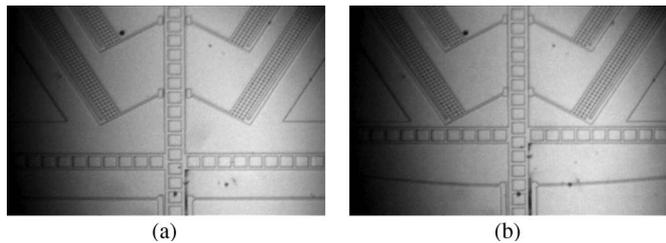

(a) (b)

Fig. 9. (a) Shuttle at zero displacement. (b) Shuttle displaced by 170 μm, with a maximum speed of 350 μm/s and an initial step size of about 10 μm.

to create an optical path for the 850-nm-wavelength VCSEL and to remove the substrate plane below the lens shuttle to minimize surface stiction issues. Hydrofluoric acid vapor (HF vapor) is used to etch the oxide layer and release the MEMS structures. The commercially purchased bulk lens is fastened to the MEMS shuttle with an ultraviolet curable optical adhesive.

Electrical testing of the device was conducted through a PCB board wire bonded directly to the silicon on the MEMS device. A 32 input/output digital DAQ board with software control is used to output the voltages to the devices. A total of nine independent digital channels are required for the full operation of the device. Because all thermal actuators are identical, a constant-voltage digital signal is used for the operation of the entire device.

V. EXPERIMENTAL RESULTS AND ANALYSIS

Still frame images of the shuttle displaced by 170 μm with a peak velocity of 350 μm/s and an initial step size of about 10 μm by the thermal actuators are shown in Fig. 9. The maximum displacement is limited by the anchors, as shown above the shuttle frame. Fig. 10 shows the brake system disengaging and engaging the brake pads via pairs of electrothermal actuators. Images of the shuttle being held by the brakes are shown in Fig. 11; when the brake is disengaged, the shuttle releases back to its equilibrium state. These images were taken from a single device where all actuators were functioning simultaneously.
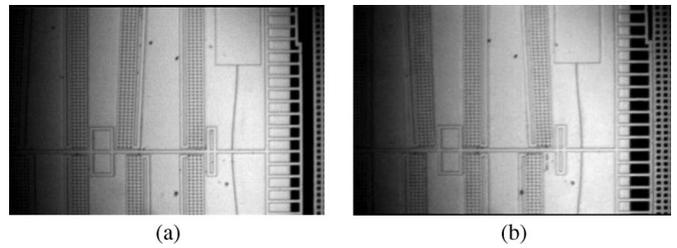

(a) (b)

Fig. 10. (a) Bistable brake switched to the "open" state by two thermal actuators (only one is shown). (b) Brake switched to the "closed" state, by two different thermal actuators.
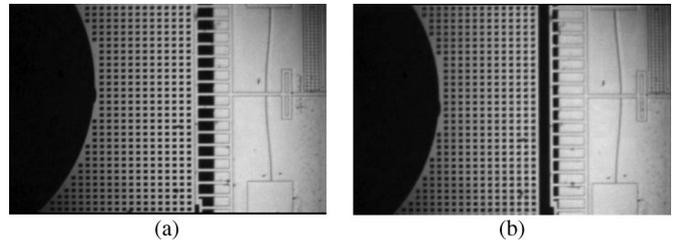

(a) (b)

Fig. 11. (a) Shuttle is held with a displacement of 60 μm by the stepper actuators. (b) Once the brake is released, the shuttle falls back to its equilibrium state.
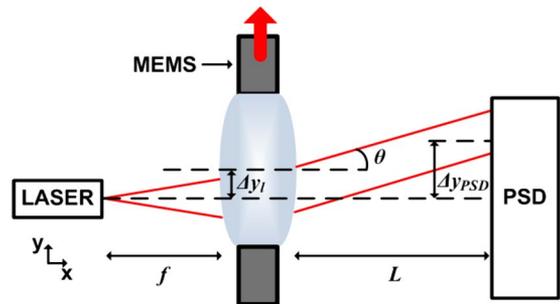

Fig. 12. Optical setup used to obtain high-resolution displacement plots of the lens scanner.

Once the MEMS components were verified to be working, the lens was mounted onto the MEMS device to test optical steering and interconnect capabilities. With an 850-nm VCSEL placed at the back focal plane of the integrated MEMS/lens system, we are able to measure high-resolution position information of the lens scanner by using a position sensing detector (PSD), as shown in Fig. 12. Absolute position values of the lens are back calculated using the measured distance of the lens to the PSD. Please note that all PSD data correspond to the device in the vertical orientation, as in Fig. 12.

Fig. 13 shows the measured high-resolution real-time displacement of the MEMS/lens shuttle system by the stepper actuators. As the voltages are increased from 25 to 30 V, the maximum displacements are also increased from 40 to 68 μm. The total lens displacement is reduced when compared to the video images due to actuator fatigue; further analysis is discussed in Section VII. When the bistable brakes are engaged, the shuttle displacement is completely flat (4 s $< t <$ 4.6 s) and is comparable to the case when neither actuators nor brakes are in use (4.9 s $< t <$ 5.6 s). The second half of the data corresponds to the shuttle moving downward, in the same
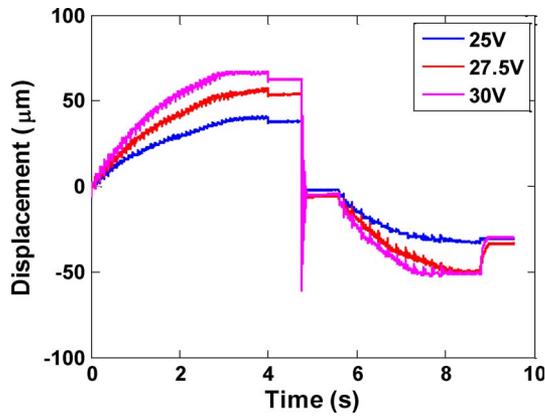
Fig. 13. Measured displacement of the MEMS/lens system with varied applied voltages with 50-ms step time. The upward sloping portion (t < 4 s) corresponds to the top set of actuators moving the lens up, against gravity. The flat region immediately following (4 s < t < 4.7 s) corresponds to the bistable brake engaged and holding the shuttle in place. The large amplitude ringing is the oscillation of the lens shuttle after the brakes are disengaged. The downward sloping portion (t > 5.6 s) corresponds to the bottom actuators moving the shuttle with gravity. The displacement appears to jump back to about −30 μm before the brakes are fully engaged. This effect is due to a faulty actuator. The last flat portion corresponds to the brakes holding the shuttle in place.

direction as gravity, thus the negative displacement values. The magnitude of the downward displacement is smaller than that of the upward displacement; this is due to a faulty actuator and can be seen by the less ideal displacement plot.

A more detailed look and explanation of the 30-V stepper data are shown in Fig. 14. As the displacement of the shuttle increases, the individual step heights change, even becoming negative at high displacements, as shown in Fig. 14(c). The oscillation of the MEMS shuttle and suspension springs, shown in Fig. 14(d), shows a resonance of 50 Hz. Assuming that the lens mass is the dominant mass, the spring constant of the suspension springs can be back calculated to be 4.44 N/m, almost a factor of two smaller than originally designed. This is attributed to the undesired overetching of the DRIE process.

Given the spring stiffness, the maximum pushing force of a healthy pair of actuators can be calculated, assuming a displacement of 170 μm, to be $F_{\mathrm{act},y} = 0.75$ mN at 30 V in the shuttle direction, which translates to a magnitude of about $F_{\mathrm{act}} = 1$ mN in actuator force along the displacement direction, as shown in Fig. 4. Using the measured actuator/shuttle coupled resonant frequency of 230 Hz from Fig. 14(a)–(c), we calculate the stiffness to be 102 N/m for a pair of actuators engaged with the shuttle. With the actuator stiffness and total force magnitude, we calculate that the step size should be about 10 μm, which agrees well with the video data. The individual step sizes measured in Fig. 13 are about one-fourth of the step size obtained from the video data due to actuator fatigue; a more detailed discussion is provided in Section VII. Simulations of the actuator/shuttle system, with a pivoting foot, show a stiffness of 145 N/m; however, due to overetching, the experimental stiffness is lower in comparison. The actuator/shuttle stiffness can be tuned by adjusting the dimensions of the leg coming off of the actuator. For example, if smaller step sizes are desired, it is best to adjust the dimensions so as to increase the stiffness of the leg.
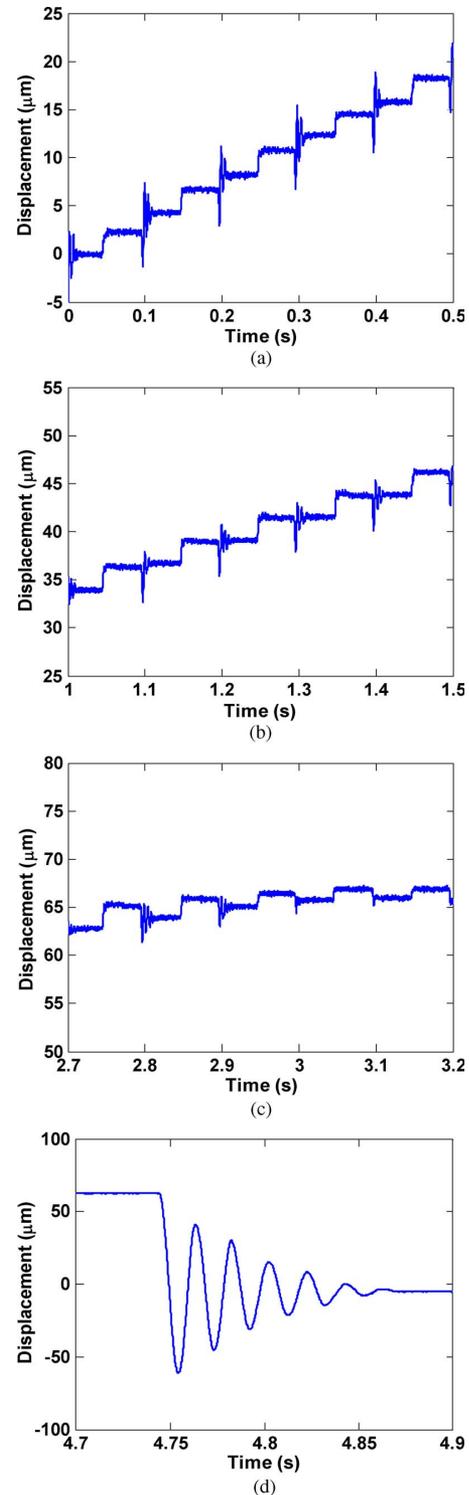

Fig. 14. Close-up view of the 30-V stepper data with $t_s = 50$ ms previously shown in Fig. 13. (a) shows the data in the time range 0 s < t < 0.5 s. We see that, with each actuator step, the shuttle is displaced by about 2.5 μm. With every other step, we see a ringing of about 230 Hz, which occurs when the stepper transitions from two pairs of actuators to one pair. (b) shows the data in the time range 1 s < t < 1.5 s. Only when two actuators are engaged does the shuttle move upward; otherwise, when only a single pair is engaged, the shuttle remains in place. (c) shows the data in the time range 2.7 s < t < 3.2 s. When both actuators are engaged, we still obtain a positive displacement; however, when only a single pair is engaged, the shuttle moves slightly backward. (d) shows the data in the time when the brakes are disengaged and the entire shuttle oscillates freely, revealing the resonant frequency of the suspension spring/lens system to be 50 Hz.
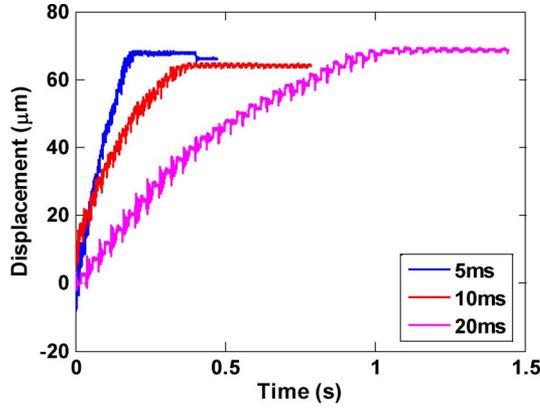
Fig. 15. Displacement data at different step time periods with a step voltage of 32.5 V. As the time step is decreased, the overall actuator velocity is increased.
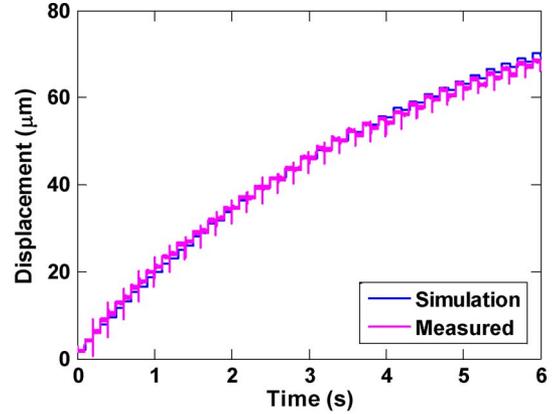

Fig. 16. Simulated stepper displacement curve compared to measured data at 100-ms stepper time. The simulated data are modeled from the 50-ms stepper data. The close comparison between the two shapes confirms the validity of the model.

The step time width t_s of the actuators is varied to adjust the rate of the shuttle displacement, as shown in Fig. 15. We find the minimum step time to be around 5 ms, which corresponds to the thermal dissipation time constant of the thermal actuators. For time periods less than this limit, the actuators do not have enough time to cool down and pull back, preventing the stepper motor from functioning. In the 5- and 10-ms data, we can no longer see discrete steps; this is due to the long settling time of the stepper and the short duration of each step.

VI. MODELING

A basic steady-state model is presented to better understand the mechanics of the stepper motor. In the data, we see a stair-step displacement curve corresponding to the stepping voltage pattern. For the case when a single pair of actuators is engaged with the shuttle, we calculate the displacement of the shuttle at discrete steps with the following empirical equation:

$$y(n) - y(n-1) = \frac{F_a - k_s y(n-1)}{k_s + k_a} \qquad (1)$$

where $y(n)$ is the height of the actuator at step n, F_a is the force due to a single pair of actuators, k_s is the shuttle suspension spring constant, and k_a is the spring constant of the shuttle/actuator system. For the case of two pairs of actuators, we obtain the following equation:

$$y(n) - y(n-1) = \frac{F_a}{k_s + k_a}. \qquad (2)$$

We can see that (2) does not have the shuttle suspension component in the numerator. This is derived empirically and can be intuitively interpreted as the first engaged pair effectively canceling out the restoring force of the shuttle suspension. We observed experimentally that the displacement of the second step remained relatively constant throughout the entire movement of the shuttle and was thus independent of the shuttle springs. As a result, we can drop the shuttle component and are left with (2). Using the parameters extracted from the measured data ($k_s = 4.44$ N/m and $k_a = 102$ N/m), and fitted values for the reduced actuator force due to fatigue ($F_a = 0.216$ mN),

we created a computer program to simulate the displacement plots shown in Fig. 16. The model curve is in relatively good agreement with the measured data, considering the first-order model.

VII. LONG-TERM TESTING

For blade server consumer applications, the long-term reliability of the device is tested to ensure that it can function properly over the lifetime of the product. Several components were operated and observed over a period of two months, including the bistable structure, brake pad, and stepper foot pad. The bistable structure showed no noticeable degradation during the operating period and never failed to achieve both states when enough force was applied. Surprisingly, issues with stiction were also rarely observed anywhere on the device. Some causes for this desirable effect are suspected to be the HF vapor etch step, nonflat/parallel surfaces due to DRIE etching, and high actuator forces. However, the large size and mass of the lens do cause the overall device to be very sensitive to high accelerations, for example, devices did break due to the dropping of the device on a table. This undesired effect can be mitigated with proper packaging to prevent the shuttle from displacing beyond the fracture stress limit of the silicon springs.

A concern for most users would be the frictional contacts (brake and stepper foot pad) with the main lens shuttle. Fig. 17 shows microscope images of stepper and brake pad teeth before and after long-term use of about 1 million actuations. The stepper teeth only show physical brandishing on the pivot points that make contact with the shuttle, as in Fig. 17(b). The opposite corner shows almost no damage. The brake pad teeth show almost no brandishing and appear to withstand the long-term testing results. During normal operation, slipping of the stepper or brake was almost never observed and proved to be reliable over the duration of the tests.

The primary risk of failure for long-term testing comes from the electrothermal actuators themselves, as was previously reported for surface-micromachined U-shaped thermal actuators
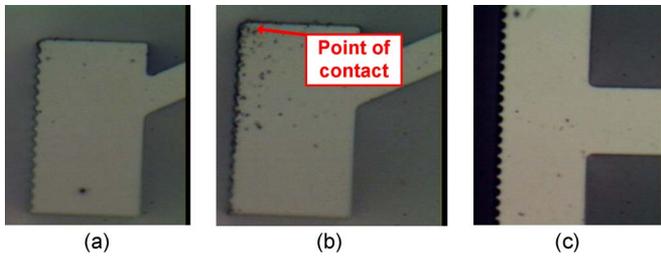
Fig. 17. Microscope images of the teeth for long-term-reliability frictional testing. (a) Unused and clean stepper teeth. (b) Stepper teeth after prolonged use. The point of contact refers to the corner of which the stepper makes contact with the shuttle. (c) Brake teeth showed very little sign of wear and tear as all of the teeth looked relatively intact.
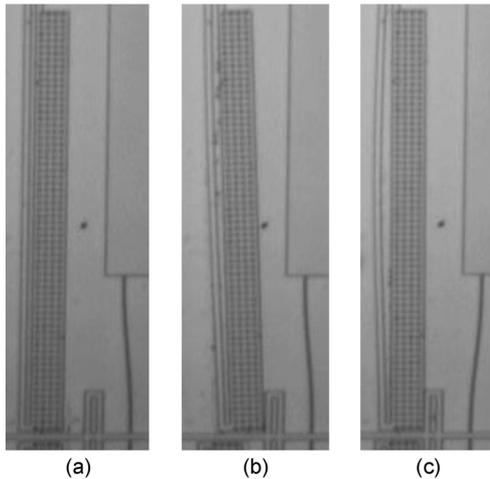

Fig. 18. Thermal actuator comparison with free bending and pushing a rigid structure. (a) Initial state of thermal actuator with zero current. (b) Actuator at 35 V with free bending; the bending of the hot arm is small. (c) Actuator at 35 V pushing against the bistable structure; we can see that the bending of the hot arm is more severe.

[36]. The primary cause of actuator force degradation is from structural deformation of the hot arm of the thermal actuator. When the current, and thus temperature, is high enough, the hot arm expands significantly and can be permanently deformed. This causes the actuator to change its initial cold shape from a straight beam to a slightly bent structure when no current is applied, as in Fig. 19(c). If the current is kept low such that no major deformation of the hot arm is observable, then no degradation in force was observed after 3.5 million actuations, although with lower current comes lower total absolute force. However, the higher the current, the lower the expected lifetime of the actuator, as was previously reported. Therefore, there is a tradeoff between actuation force and lifetime.

In terms of long-term reliability, there is an important difference between the tests done in [36] and the actuators used for a stepper motor. Previous tests used U-shaped thermal actuators in a free-displacing method, meaning that the actuators were not used to push against anything and were free to bend to their maximum displacement, as in Fig. 18(b). For our system, the actuators push against rigid structures and, as a result, are not allowed to bend to their maximum displacement, as in Fig. 18(c). As a result, the thin hot arm is now the least stiff structure and bends more at the same current when compared
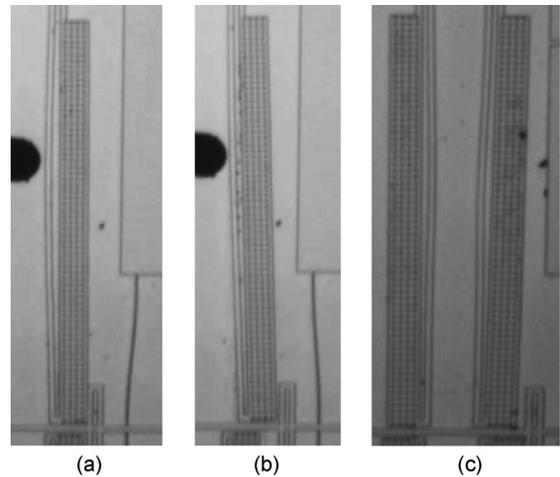

Fig. 19. (a) Single actuator at 35 V is shown and is unable to flip the bistable structure. (b) Black circle is a rigid probe tip and is pressed against the bulging region of the hot arm, and clearly, the force is dramatically increased as the actuator has enough force to flip the bistable structure. (c) Long-term permanent deformation of the actuators with 0 V.

to a free-bending U-shaped thermal actuator. Because of the large bending of the hot arm, actuators used for pushing rigid objects are more prone to failure at the same current than free-displacing actuators. Since a portion of the energy is used to bend the hot arm, the overall pushing force of the entire actuator is reduced which can impact the performance of the device, as was observed in the high-resolution PSD data from earlier.

A method to mitigate the effects of pushing rigid bodies on the reliability and maximum pushing force is to prevent the hot arm from taking on the bending shape. A probe was used to act as a rigid structure to prevent the hot arm from undesirable bending, thus preventing the permanent structural deformation. The rigid probe tip also serves to act as a leverage point and thus significantly improves the pushing force of the actuator, as shown in Fig. 19(b). The probe tip and actuator solution show no sign of permanent deformation after 6.9 million actuations; however, when no probe is present, permanent large deformation occurs around 1.7 million actuations. For future designs, it would be advantageous to have a rigid body next to the hot arm so as to act as both a leverage point and prevention for deformation. This can be easily achieved by leaving an etched block of silicon next to the actuator.

VIII. FREE-SPACE OPTICAL LINK TEST

To demonstrate active optical alignment, a telecentric optical setup was constructed with the MEMS lens scanner, 10-G VCSEL chip, and 10-Gb/s free-space PD, as shown in Fig. 20. The VCSEL chip is bonded to a copper block with silver epoxy to create a heat sink. A 10-Gb/s RF probe is then mounted sideways to make contact with the VCSEL chip. The receiving lens used in our setup has dimensions of $f_1 = 13.86$ mm and $d = 2.8$ mm. When the receiving board is tilted by $0.45°$, the eye diagram is closed, as in Fig. 21(a). However, when we scan the lens up by 49 μm, we regain connection, and the eyes become open, as in Fig. 21(b).
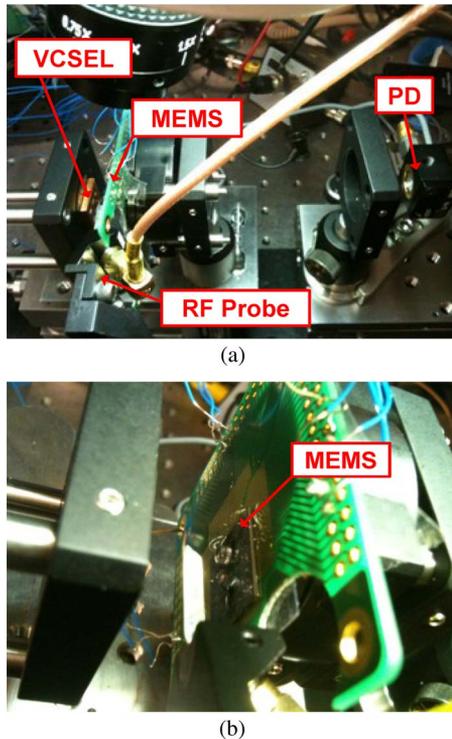
Fig. 20. (a) Optical table setup for the board-to-board experiment, with the copper-mounted VCSEL chips on the left and the high-speed PD on the right. (b) Close-up look of the MEMS chip mounted on a PCB board, wire bonded, and soldered.
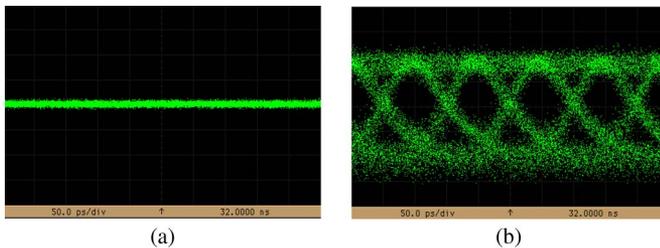

Fig. 21. (a) Board is tilted by $0.45°$, and the signal is lost. (b) After the lens is displaced by 49 μm, the tilt is corrected and the link is reestablished.

IX. CONCLUSION

The successful design, characterization, reliability testing, and full system integration of an electrothermal stepper motor-based lens scanner for free-space board-to-board optical interconnects have been demonstrated. A maximum lens shuttle displacement of 170 μm with a measured healthy actuator pushing force of 0.75 mN is shown. However, due to actuator fatigue, the measured pushing force of the deformed actuator decreased to 0.216 mN. Long-term reliability tests revealed the main source of failure to be the deformation of the actuators themselves, thus causing the decreased actuator pushing force. A possible solution is presented to help mitigate these effects and increase both reliability and pushing force. The optical MEMS system is capable of correcting a $0.45°$ tilt with fatigued actuators, as well as lateral displacements in the X-, Y-, and Z-directions, beyond the error magnitudes expected in real-world board-to-board systems. The maximum correctable tilt can be increased by implementing rigid structures to help prevent the actuators from deforming.

REFERENCES

[1] G. Astfalk, "Why optical data communications and why now?" *Appl. Phys. A, Mater. Sci. Process.*, vol. 95, no. 4, pp. 933–940, Jun. 2009.

[2] D. Miller, "Device requirements for optical interconnects to silicon chips," *Proc. IEEE*, vol. 97, no. 7, pp. 1166–1185, Jul. 2009.

[3] M. J. Crippen, R. K. Alo, D. Champion, R. M. Clemo, C. M. Grosser, N. J. Gruendler, M. S. Mansuria, J. A. Matteson, M. S. Miller, and B. A. Trumbo, "BladeCenter packaging, power, and cooling," *IBM J. Res. Develop.*, vol. 49, no. 6, pp. 887–904, Nov. 2005.

[4] H. Kuo, P. Rosenberg, R. Walmsley, S. Mathai, L. Kiyama, J. Straznicky, M. Mclaren, M. Tan, and S.-Y. Wang, "Free-space optical links for board-to-board interconnects," *Appl. Phys. A, Mater. Sci. Process.*, vol. 95, no. 4, pp. 955–965, Jun. 2009.

[5] J.-H. Yeh and R. K. Kostuk, "Free-space holographic optical interconnects for board-to-board and chip-to-chip interconnections," *Opt. Lett.*, vol. 21, no. 16, pp. 1274–1276, Aug. 1996.

[6] F. Wu, L. Vj, M. S. Islam, D. A. Horsley, R. G. Walmsley, S. Mathai, D. Houng, M. R. T. Tan, and S.-Y. Wang, "Integrated receiver architectures for board-to-board free-space optical interconnects," *Appl. Phys. A*, vol. 95, no. 4, pp. 1079–1088, Feb. 2009.

[7] E. M. Strzelecka, D. A. Louderback, B. J. Thibeault, G. B. Thompson, K. Bertilsson, and L. A. Coldren, "Parallel free-space optical interconnect based on arrays of vertical-cavity lasers and detectors with monolithic microlenses," *Appl. Opt.*, vol. 37, no. 14, pp. 2811–2821, May 1998.

[8] T. Sakano, T. Matsumoto, and K. Noguchi, "Three-dimensional board-to-board free-space optical interconnects and their application to the prototype multiprocessor system: COSINE-III," *Appl. Opt.*, vol. 34, no. 11, pp. 1815–1822, Apr. 1995.

[9] D. V. Plant, M. B. Venditti, E. Laprise, J. Faucher, K. Razavi, M. Teauneuf, A. G. Kirk, and J. S. Ahearn, "256-channel bidirectional optical interconnect using VCSELs and photodiodes on CMOS," *J. Lightw. Technol.*, vol. 19, no. 8, pp. 1093–1103, Aug. 2001.

[10] H. J. Zhou, V. Morozov, J. Neff, and A. Fedor, "Analysis of a vertical-cavity surface-emitting laser-based bidirectional free-space optical interconnect," *Appl. Opt.*, vol. 36, no. 17, pp. 3835–3853, Jun. 1997.

[11] J.-C. Tsai and M. C. Wu, "Design, fabrication, and characterization of a high fill-factor, large scan-angle, two-axis scanner array driven by a leverage mechanism," *J. Microelectromech. Syst.*, vol. 15, no. 5, pp. 1209–1213, Oct. 2006.

[12] B. E. Yoxall, R. Walmsley, H.-P. Kuo, S.-Y. Wang, M. Tan, and D. A. Horsley, "Two-axis MEMS lens alignment system for free-space optical interconnect," *IEEE J. Sel. Topics Quantum Electron.*, vol. 17, no. 3, pp. 559–565, May/Jun. 2011.

[13] J. Tsai and M. C. Wu, "Gimbal-less MEMS two-axis optical scanner array with high fill-factor," *J. Microelectromech. Syst.*, vol. 14, no. 6, pp. 1323–1328, Dec. 2005.

[14] H. Toshiyoshi, G.-D. J. Su, J. LaCosse, and M. C. Wu, "A surface micromachined optical scanner array using photoresist lenses fabricated by a thermal reflow process," *J. Lightw. Technol.*, vol. 21, no. 7, pp. 1700–1708, Jul. 2003.

[15] K. Takahashi, H. N. Kwon, M. Mita, K. Saruta, J.-H. Lee, H. Fujita, and H. Toshiyoshi, "A silicon micromachined $f-\theta$ microlens scanner array by double-deck device design technique," *IEEE J. Sel. Topics Quantum Electron.*, vol. 13, no. 2, pp. 277–282, Apr. 2007.

[16] S. Kwon and L. P. Lee, "Stacked two dimensional micro-lens scanner for micro confocal imaging array," in *Proc. 15th IEEE Int. Conf. Micro Electro Mech. Syst.*, 2002, pp. 483–486.

[17] J. Singh, J. H. S. Teo, Y. Xu, C. S. Premachandran, N. Chen, R. Kotlanka, M. Olivo, and C. J. R. Sheppard, "A two axes scanning SOI MEMS micromirror for endoscopic bioimaging," *J. Micromech. Microeng.*, vol. 18, no. 2, p. 025 001, Feb. 2008.

[18] M. Sasaki, F. Bono, and K. Hane, "XY-stage for scanning media for optical data storage," in *Proc. IEEE/LEOS Int. Conf. Opt. MEMS, Appl. Conf.*, 2006, pp. 36–37.

[19] W. Piyawattanametha, P. R. Patterson, D. Hah, H. Toshiyoshi, and M. C. Wu, "Surface- and bulk-micromachined two-dimensional scanner driven by angular vertical comb actuators," *J. Microelectromech. Syst.*, vol. 14, no. 6, pp. 1329–1338, Dec. 2005.

[20] K. Yu, N. Park, D. Lee, and O. Solgaard, "Superresolution digital image enhancement by subpixel image translation with a scanning micromirror," *IEEE J. Sel. Topics Quantum Electron.*, vol. 13, no. 2, pp. 304–311, Apr. 2007.

[21] L. Zhou, J. M. Kahn, and K. S. Pister, "Scanning micromirrors fabricated by an SOI/SOI wafer-bonding process," *J. Microelectromech. Syst.*, vol. 15, no. 1, pp. 24–32, Feb. 2006.

[22] H. Choo and R. S. Muller, "Addressable microlens array to improve dynamic range of Shack–Hartmann sensors," *J. Microelectromech. Syst.*, vol. 15, no. 6, pp. 1555–1567, Dec. 2006.

[23] K. Hedsten, J. Melin, J. Bengtsson, P. Modh, D. Karlén, B. Löfving, R. Nilsson, H. Rödjegård, K. Persson, P. Enoksson, F. Nikolajeff, and G. Andersson, "MEMS-based VCSEL beam steering using replicated polymer diffractive lens," *Sens. Actuators A, Phys.*, vol. 142, no. 1, pp. 336–345, Mar. 2008.

[24] D. Hah, C.-A. Choi, C.-K. Kim, and C.-H. Jun, "A self-aligned vertical comb-drive actuator on an SOI wafer for a 2D scanning micromirror," *J. Micromech. Microeng.*, vol. 14, no. 8, pp. 1148–1156, Aug. 2004.

[25] J. Chou, K. Yu, T. Bakhishev, D. Horsley, R. Walmsley, S. Mathai, M. Tan, S. Y. Wang, V. Subramanian, and M. Wu, "Rotational optical alignment for array based free space board-to-board optical interconnect with zero power hold," in *Proc. IEEE 23rd Int. Conf. MEMS*, 2010, pp. 807–810.

[26] J. Chou, K. Yu, D. Horsley, B. Yoxall, S. Mathai, M. Tan, S.-Y. Wang, and M. Wu, "Robust free space board-to-board optical interconnect with closed loop MEMS tracking," *Appl. Phys. A, Mater. Sci. Process.*, vol. 95, no. 4, pp. 973–982, Jun. 2009.

[27] M. Naruse, S. Yamamoto, and M. Ishikawa, "Real-time active alignment demonstration for free-space optical interconnections," *IEEE Photon. Technol. Lett.*, vol. 13, no. 11, pp. 1257–1259, Nov. 2001.

[28] R. Legtenberg, A. W. Groeneveld, and M. Elwenspoek, "Comb-drive actuators for large displacements," *J. Micromech. Microeng.*, vol. 6, no. 3, pp. 320–329, Sep. 1996.

[29] J. Qiu, J. H. Lang, A. H. Slocum, and A. C. Weber, "A bulk-micromachined bistable relay with U-shaped thermal actuators," *J. Microelectromech. Syst.*, vol. 14, no. 5, pp. 1099–1109, Oct. 2005.

[30] R. Yeh, S. Hollar, and K. S. J. Pister, "Single mask, large force, and large displacement electrostatic linear inchworm motors," *J. Microelectromech. Syst.*, vol. 11, no. 4, pp. 330–336, Aug. 2002.

[31] J. H. Comtois and V. M. Bright, "Applications for surface-micromachined polysilicon thermal actuators and arrays," *Sens. Actuators A, Phys.*, vol. 58, no. 1, pp. 19–25, Jan. 1997.

[32] M. Pai and N. C. Tien, "Low voltage electrothermal vibromotor for silicon optical bench applications," *Sens. Actuators A, Phys.*, vol. 83, no. 1–3, pp. 237–243, May 2000.

[33] J. M. Maloney, D. S. Schreiber, and D. L. DeVoe, "Large-force electrothermal linear micromotors," *J. Micromech. Microeng.*, vol. 14, no. 2, pp. 226–234, Feb. 2004.

[34] J. D. Grade, K. Y. Yasumura, and H. Jerman, "Micromachined actuators with braking mechanisms," *Sens. Actuators A, Phys.*, vol. 122, no. 1, pp. 1–8, Jul. 2005.

[35] T. Overstolz, P. A. Clerc, W. Noell, M. Zickar, and N. F. de Rooij, "A clean wafer-scale chip-release process without dicing based on vapor phase etching," in *Proc. 17th IEEE Int. Conf. MEMS*, 2004, pp. 717–720.

[36] R. A. Conant and R. S. Muller, "Cyclic fatigue testing of surface-micromachined thermal actuators," in *Proc. ASME Int. Mech. Eng. Congr. Expo.*, Nov. 1998, pp. 15–20.

Jeffrey B. Chou received the B.S., M.S., and Ph.D. degrees in electrical engineering and computer sciences from the University of California at Berkeley in 2007, 2010, and 2011, respectively.

In 2010, he was the Cofounder of the MEMS start-up company Anoka Microsystems Inc., which focuses on designing and manufacturing MEMS-based optical switches. He is currently with the Department of Electrical Engineering and Computer Sciences, University of California at Berkeley.

Dr. Chou was a recipient of the National Defense and Science Engineering Graduate Fellowship in 2009.

Kyoungsik Yu received the B.S. degree from Seoul National University, Seoul, Korea, in 1999, and the M.S. and Ph.D. degrees in electrical engineering from Stanford University, Stanford, CA, in 2001 and 2004, respectively.

He was a Postdoctoral Researcher at the University of California at Berkeley before joining the Department of Electrical Engineering, Korea Advanced Institute of Science and Technology, Daejeon, Korea, as an Assistant Professor in 2010. His current research interests are applications of (sub)wavelength-scale optoelectronic devices and systems for photonic interconnects, optical imaging, and sensing.

Ming C. Wu (S'82–M'83–SM'00–F'02) received the Ph.D. degree from the University of California at Berkeley in 1988.

He is a Professor of electrical engineering and computer sciences at the University of California at Berkeley. Before joining the faculty of the University of California, he was a member of Technical Staff at AT&T Bell Laboratories, Murray Hill, NJ (1988–1992), and a Professor of electrical engineering at the University of California at Los Angeles (1992–2004). He has published seven book chapters, over 200 journal papers, and 300 conference papers. He is the holder of 20 U.S. patents. His research interests include microelectromechanical systems, MOEMS, optoelectronics, and nanophotonics.

Dr. Wu was a Packard Foundation Fellow (1992–1997). He is a member of the Optical Society of America, and was a recipient of its 2007 Paul F. Forman Engineering Excellence Award.